ROYAL SOCIETY
OF CHEMISTRY

## TECHNICAL NOTE

Check for updates

# Simultaneous determination of Sm–Nd isotopes, trace-element compositions and U–Pb ages of titanite using a laser-ablation split-stream technique with the addition of water vapor†

Le Zhang, [iD] *[a] Jia-Lin Wu,[b] Yan-Qiang Zhang,[a] Ya-Nan Yang,[a] Peng-Li He,[a] Xiao-Ping Xia [iD] [a] and Zhong-Yuan Ren[a]

Titanite is a widespread accessory nesosilicate with high trace-element contents including rare-earth elements, Th, and U, and is thus suitable for *in situ* isotopic and trace-element analyses and U–Pb dating. Here we describe a laser-ablation split-stream technique for simultaneously determining Sm–Nd isotopes, trace-element compositions and U–Pb ages in titanite. A laser ablation system was connected to multi-collector (MC) and sector field (SF) inductively coupled plasma–mass spectrometry (ICP–MS) systems. The laser-ablated aerosol was split into two gas streams and transported simultaneously to the MC–ICP–MS system for Sm–Nd isotope analysis and to the SF–ICP–MS system for trace-element analysis and U–Pb dating. A small flow of water vapor was introduced to the gas stream after the LA chamber to improve the sensitivity of Nd (by 40%) on MC–ICP–MS and to maintain oxide yields at low levels for SF–ICP–MS trace-element analyses. Three well-constrained reference titanite standards (T3, OLT1, and Ontario) were analysed to evaluate precision and accuracy. Resulting Sm–Nd isotopic and trace-element compositions and U–Pb ages were consistent with recommended values. The method was applied in simultaneously determining Sm–Nd isotopes, trace-element compositions and U–Pb ages for titanite from the Manjinggou marble of the North China Craton.

## 1. Introduction

Titanite ($CaTiSiO_4O$) is a common accessory nesosilicate with widespread occurrence in a range of igneous, metamorphic, sedimentary, and hydrothermal rocks related to ore deposits.[1,2] Due to its high U contents (10–1000 $\mu g\ g^{-1}$) and the high closure temperature of the U–Pb system (660–750 °C),[1,3–6] titanite provides a useful U–Pb geochronometer, especially for alkaline igneous rocks[7–9] and hydrothermal ore deposits.[10–13] In metamorphic rocks, titanite together with other accessory minerals such as zircon and rutile with different U–Pb closure temperatures is used to constrain the pressure–temperature–time history of metamorphic terranes.[14–16] The sevenfold Ca coordination site in titanite promotes the incorporation of rare-earth elements (REEs),[1] allowing the possibility of *in situ* Sm–Nd isotope analysis.[8,17,18] Due to the high closure temperature of the Sm–Nd isotopic system (850–950 °C) in titanite, the original Sm–Nd isotopic composition may survive high-temperature metamorphism.[19] The trace-element geochemistry of titanite also provides information about its crystallisation temperature and pressure[15,20] and oxygen fugacity conditions.[21,22] Although analysis by isotope dilution–thermal ionisation mass spectrometry (ID–TIMS) is considered the most precise U–Pb dating method for U-bearing minerals,[23–26] *in situ* analyses by laser ablation–inductively coupled plasma–mass spectrometry (LA–ICP–MS) or secondary ion mass spectrometry (SIMS) are the most widely applied, requiring relatively simple sample preparation and yielding detailed age information based on complicated mineral growth zoning, which is not accessible when doing full chemical digest in ID-TIMS analysis.[11,27–31] Compared to SIMS, which is sensitive to crystal orientation and requires high-quality polished sample surface,[32–34] sample preparation for LA-ICP-MS analysis is much simpler and faster.

Traditionally, *in situ* titanite U–Pb dating and Sm–Nd isotopic and trace-element analyses are undertaken separately in three independent analytical runs with Sm–Nd analyses involving only LA–multicollector (MC)–ICP–MS. In some studies, U–Pb dating and trace-element analyses have been undertaken in a single LA–ICP–MS run.[10,15,35] Analyses of Sm–Nd isotopes and trace-elements usually involve different single-crystal domains to those used for U–Pb dating, and the resulting data may not be strictly correlative, as titanite zonation may vary with age and composition. Thanks to the LA split-stream

[a]State Key Laboratory of Isotope Geochemistry, CAS Center for Excellence in Deep Earth Science, Guangzhou Institute of Geochemistry, Chinese Academy of Sciences, Guangzhou 510640, China. E-mail: zhangle@gig.ac.cn

[b]School of Earth Science and Resources, Chang'an University, Xi'an 710054, China
† Electronic supplementary information (ESI) available. See DOI: 10.1039/d1ja00246e

**Table 1** Summary of the instrumental operating conditions

| Mass spectrometry parameters | | |
| --- | --- | --- |
| Instrument | Neptune Plus | Element XR |
| RF forward power | 1250 W | 1200 W |
| Cool gas | 16 L min$^{-1}$ | 16 L min$^{-1}$ |
| Auxiliary gas | 0.95 L min$^{-1}$ | 0.8 L min$^{-1}$ |
| Sample gas | 0.94 L min$^{-1}$ | 0.9 L min$^{-1}$ |
| Sample cones | H cone Ni | H cone Ni |
| Skimmer cones | X cone Ni | H cone Ni |
| Integration time | 0.262 s | |
| Mass resolution | Low | Low |
| Amplifier | 10$^{11}$ Ω | |
| Measurement | Sm–Nd isotopes | U–Pb dating and trace elements |
| Sample time | | 0.003 s for all masses |
| Settling time | | $^{29}$Si 0.3 s, $^{88}$Sr 0.064 s, $^{139}$La 0.034 s, $^{181}$Ta 0.023 s, $^{238}$U 0.027 s; all other masses used 0.001 s |

| Laser ablation system | |
| --- | --- |
| Instrument | RESOlutin M-50 |
| Wavelength | UV 193 nm |
| Energy density | 4 J cm$^{-2}$ |
| Ablation type | Spot |
| Spot size | 33–82 μm |
| Carrier gas | Helium 0.4 L min$^{-1}$ |
| Pulse rate | 6–10 Hz |
| Ablation time | 35 s |

(LASS) technique,[36,37] it is possible to simultaneously analyze high precise isotopic ratios, U–Pb age and elemental datasets for the same micro-analytical volume in a single run.[38–41] In the LASS technique, an LA system ablates the sample to produce aerosol, which is split into two gas lines, with one being transferred to an MC–ICP–MS system for isotopic ratio determination (*e.g.*, Nd isotopes in titanite and apatite, or Hf isotopes in zircon and rutile) and the other to a single-collector ICP–MS for U–Pb dating and/or trace-element analysis.[39,41–45]

However, LASS aerosol splitting reduces the signal intensity in both MS systems,[37,42] which may lead to loss of precision, especially for isotope analyses. This could be overcome by use of more-powerful LA conditions (*e.g.*, large spot size and high repetition rate) or improvement in instrumental sensitivity. However, minerals with complicated zonation structures require high-spatial-resolution analysis, and larger laser spot sizes and higher repetition rates may result in composition mixing across different zones. Recent studies have demonstrated that the addition of a small flow of water vapor to the LA carrier-gas line can increase quadruple (Q) ICP–MS instrumental sensitivity and suppress elemental fractionation.[46–51] Here we investigated the effect of water vapor on MC–ICP–MS analyses, including sensitivity, oxide yield and memory effect. Water vapor addition was then applied to the LASS technique in the simultaneous determination of Sm–Nd isotopes, trace-element compositions and U–Pb dating of titanite, with improved precision for Sm–Nd isotopic data. Finally, the technique was applied to titanite from the Manjinggou marble of the North China Craton.

## 2. Experimental

### 2.1. Instrumentation

Equipment used in this study included a 193 nm LA system (RESOlution M50; Applied Spectra, USA) connected to an MC–ICP–MS system (Neptune Plus; Thermo Fisher Scientific, USA) and a single-collector sector-field (SF)–ICP–MS system (Element XR; Thermo Fisher Scientific, USA), all at the State Key Laboratory of Isotope Geochemistry, Guangzhou Institute of Geochemistry, Chinese Academy of Sciences, Guangzhou, China. Detailed descriptions of the instruments are provided
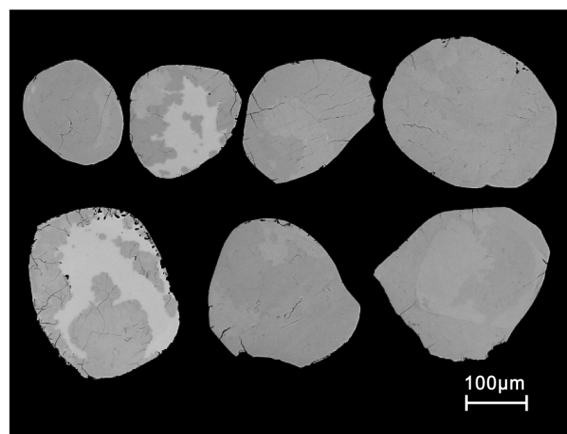


**Fig. 1** Back scatter electronic (BSE) images showing the growth texture of the representative titanite grains from the Manjinggou marble.

This journal is © The Royal Society of Chemistry 2021

*J. Anal. At. Spectrom.*, 2021, **36**, 2312–2321 | **2313**

elsewhere.[31,45] The LA conditions involved a repetition rate of 6–10 Hz with a fluence of ~4 J cm$^{-2}$. The laser spot size was 33–82 μm depending on the titanite Nd content required to obtain sufficient Nd intensity (>0.6 V on $^{143}$Nd) for high-precision Nd MC–ICP–MS isotope analysis. Each spot analysis included 30 s gas blank collection and 35 s sample signal collection. For MC–ICP–MS Sm–Nd isotope analyses, seven Faraday cups were used to detect $^{143}$Nd, $^{144}$(Nd + Sm), $^{145}$Nd, $^{146}$Nd, $^{147}$Sm, $^{148}$Nd, and $^{149}$Sm in static mode. Both $^{146}$Nd and $^{147}$Sm gas blanks were <0.2 mV. For U–Pb dating and trace-element analyses by SF–ICP–MS, the following masses were detected: $^{29}$Si, $^{88}$Sr, $^{89}$Y, $^{90}$Zr, $^{93}$Nb, $^{139}$La, $^{140}$Ce, $^{141}$Pr, $^{146}$Nd, $^{147}$Sm, $^{151}$Eu, $^{157}$Gd, $^{159}$Tb, $^{162}$Dy, $^{165}$Ho, $^{166}$Er, $^{169}$Tm, $^{174}$Yb, $^{175}$Lu, $^{178}$Hf, $^{181}$Ta, $^{202}$Hg, $^{204}$Pb, $^{206}$Pb, $^{207}$Pb, $^{208}$Pb, $^{232}$Th, and $^{238}$U. Silicon was used for internal normalisation after electron-probe microanalysis. To reduce laser-induced variations in mass fractionation, samples and the calibration standard were analysed under the same laser conditions. Details of the instrument operating conditions and settings are summarised in Table 1.

## 2.2. Samples

Four titanite reference materials (MKED1, T3, OLT1 and Ontario) and two US Geological Survey basaltic glasses (GSD-1G and BHVO-2G) were used to evaluate the analytical precision and accuracy of the LASS technique with added water vapor. MKED1 has high U (131–207 μg g$^{-1}$) and radiogenic Pb (50–93 μg g$^{-1}$) contents but a very low common-Pb content[18] and was used for external calibration in U–Pb dating by SF–ICP–MS, as well as for $^{147}$Sm/$^{144}$Nd calibration in Sm–Nd isotope analysis by MC–ICP–MS. GSD-1G, with relatively uniform trace-element contents of 40–50 μg g$^{-1}$, was used for external calibration in trace-element analyses. BHVO-2G was analysed as an unknown to evaluate the precision and accuracy of trace-element analyses. Every set of five sample analyses was followed by analysis of MKED1, BHVO-2G and GSD-1G.

This approach was applied to a suite of metamorphic titanites from the Manjinggou marble (sample number, 180803MJG1) of the Huai'an complex (North China Craton), which comprises high-pressure mafic granulite, grey gneiss, a khonalite series, granitic gneiss, and the Dapinggou garnet-bearing granite, with detailed descriptions provided by Wu et al.[52] The Manjinggou marbles are small lens-shaped bodies surrounded by pelitic and mafic granulites. The titanites are subhedral to anhedral and red-brown in colour with grain sizes of 100–300 μm. Most Manjinggou titanites exhibit uniform colour in back-scattered-electron images, although some grains have complicated structures with, for example, dark-grey cores, light-grey rims, and dendritic zoning (Fig. 1).
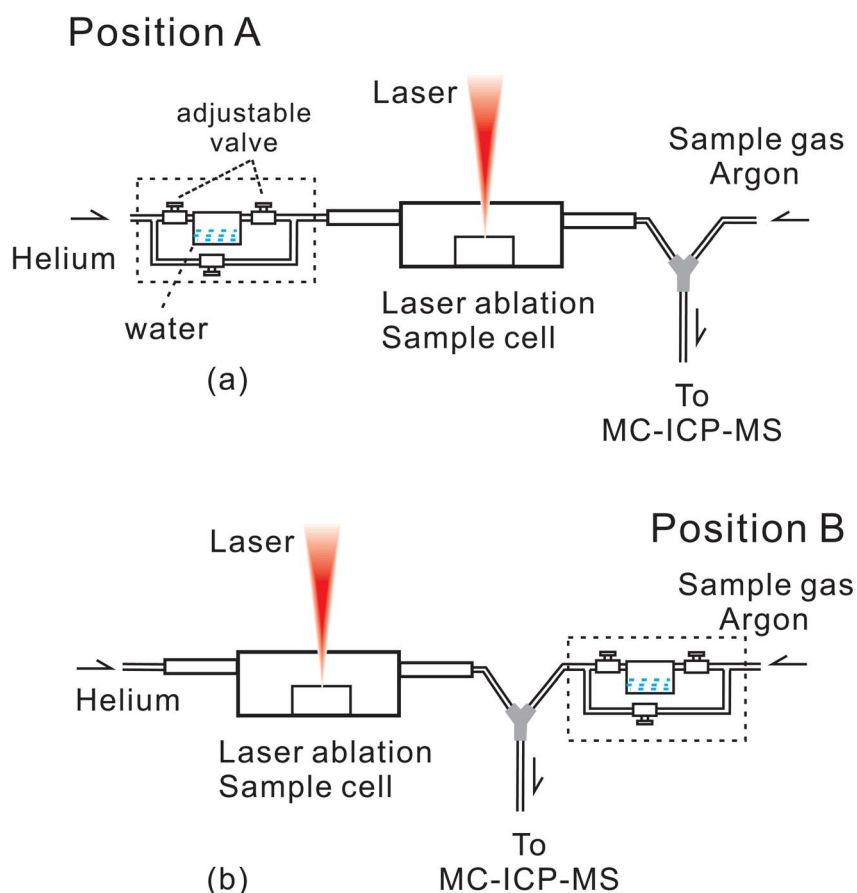


Fig. 2 The positions of the water vapor adding device on the laser gas line. (a) Before the laser ablation chamber (position A); (b) after the laser ablation chamber (position B). The part in the dotted box is the water vapor introducing device.

**2314** | J. Anal. At. Spectrom., 2021, **36**, 2312–2321

This journal is © The Royal Society of Chemistry 2021

## 2.3. Data reduction

For Sm–Nd isotope calculations, averaged gas-blank intensities were subtracted from raw time-resolved signal intensities for each measured Sm–Nd isotope. Concentrations of $^{144}$Sm, which suffers isobaric interference from $^{144}$Nd, were calculated from the $^{147}$Sm signal and the natural $^{144}$Sm/$^{147}$Sm ratio (0.20504)[53] with subtraction from the intensity of $^{144}$Sm + $^{144}$Nd. The instrumental mass biases of Sm–Nd were calculated from the measured $^{147}$Sm/$^{149}$Sm and $^{146}$Nd/$^{144}$Nd ratios and their natural ratios ($^{147}$Sm/$^{149}$Sm = 1.08507; $^{146}$Nd/$^{144}$Nd = 0.7219),[53] applying the exponential law. The isotopic fractionation of $^{147}$Sm/$^{144}$Nd was estimated using the standard (MKED1)–sample bracketing (SSB) method, with $^{147}$Sm/$^{144}$Nd = 0.1270 for MKED1.[18]

GLITTER software was used for U–Pb dating and trace-element analyses using raw data from the SSB calibration strategy, with $^{207}$Pb/$^{206}$Pb and $^{206}$Pb/$^{238}$U ratios being calculated per cycle, and $^{207}$Pb/$^{235}$U ratios from the equation $^{207}$Pb/$^{235}$U = ($^{207}$Pb/$^{206}$Pb)*($^{206}$Pb/$^{238}$U) × 137.818.[54] Uncertainty in ratios and ages for each single analysis were calculated by propagating the uncertainty of decay constants, reference material ratio uncertainty and a 2% long term variance of the validation material (MKED1) in U–Pb isotopic ratios following the uncertainty propagation protocol in Horstwood *et al.*[55] U–Pb ages and Tera–Wasserburg (TW) diagrams were produced with ISOPLOT v. 3.22 software.[56] For samples with high common-Pb contents (>1%), the $^{207}$Pb correction method[27,57] was used to correct common-Pb influence on $^{206}$Pb/$^{238}$U age. During the common lead correction, the fraction of common $^{206}$Pb ($^{206}$Pb$_{common}$) in total $^{206}$Pb ($^{206}$Pb$_{total}$) is defined as:

$$f_{206} = {}^{206}Pb_{common}/{}^{206}Pb_{total} \qquad (1)$$

In the $^{207}$Pb method, $f_{206}$ is calculated from:

$$f_{206} = ({}^{207}Pb/{}^{206}Pb_{measured} - {}^{207}Pb*/{}^{206}Pb*)/({}^{207}Pb/{}^{206}Pb_{common} - {}^{207}Pb*/{}^{206}Pb*) \qquad (2)$$

where $^{207}$Pb/$^{206}$Pb$_{measured}$ is measured $^{207}$Pb/$^{206}$Pb by mass spectrometer and $^{207}$Pb*/$^{206}$Pb* is the radiogenic $^{207}$Pb/$^{206}$Pb. $^{207}$Pb*/$^{206}$Pb* can be estimated with the following equation:

$$^{207}Pb^*/{}^{206}Pb^* = \left({}^{207}Pb/{}^{235}U\right)^* \Big/ \left({}^{206}Pb/{}^{238}U\right)^* \Big/ 137.818$$

$$= \frac{e^{\lambda_{235}t} - 1}{e^{\lambda_{238}t} - 1} \Big/ 137.818 \qquad (3)$$

where $\lambda^{235}$ and $\lambda^{238}$ are the decay constants for $^{235}$U and $^{238}$U, respectively. $t$ is sample probable age. The common lead composition ($^{207}$Pb/$^{206}$Pb$_{common}$) is estimated from Stacey and Kramers Pb evolution model[58] with sample probable age. Trace-element calibration used $^{29}$Si for internal normalisation. Time-drift correction involved linear interpolation for every five analyses based on the variation of measured signal intensity of the external standard GSD-1G.

# 3. Results and discussion

## 3.1. Effect of water vapor on LA–MC–ICP–MS analyses

Previous studies have investigated the effect of water vapor on LASS U–Pb dating with Q–ICP–MS, and this study involved mainly MC–ICP–MS with a water vapor introduction device (a quartz-glass box) modified from Luo *et al.*[49] (Fig. 2 and S1a†). The LA gas stream flowed through the glass box, mixing with water vapor produced by evaporation of Milli-Q water (Millipore, Billerica MA, USA) at room temperature. The estimated water vapor introducing speed is around 5 mL min$^{-1}$ (Fig. S1b and c†). The effects on instrumental sensitivity, oxide yield and blanks were investigated with the addition of water vapor before (position A, Fig. 2a) and after (position B, Fig. 2b) the LA chamber. Because keeping low oxide yield is important for precise trace element measurement, the oxide yields of Sr, Yb, Hf, Pb, Th and U were monitored using the in-house plagioclase
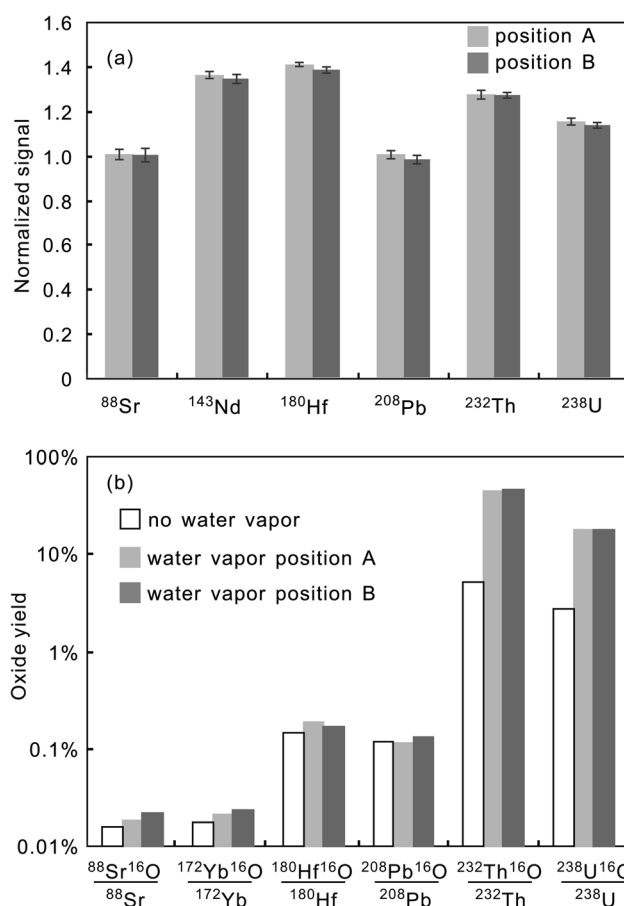


**Fig. 3** (a) Signal intensities of Sr, Nd, Hf, Pb, Th and U obtained with the addition of water vapor before and after the laser ablation chamber. The optimized signal intensities obtained under different water vapor adding positions were normalized to the signal obtained without water vapor addition. (b) Oxide yields of Sr, Yb, Hf, Pb, Th and U obtained with or without water vapor addition. All the test analyses were conducted with laser raster ablation (spot size: 45–60 μm; moving speed: 2 μm s$^{-1}$). The uncertainty bars (2 standard deviations) were calculated from three replicated analyses. The uncertainty bars for oxide yields are too small on the log coordinate plot and are not shown.
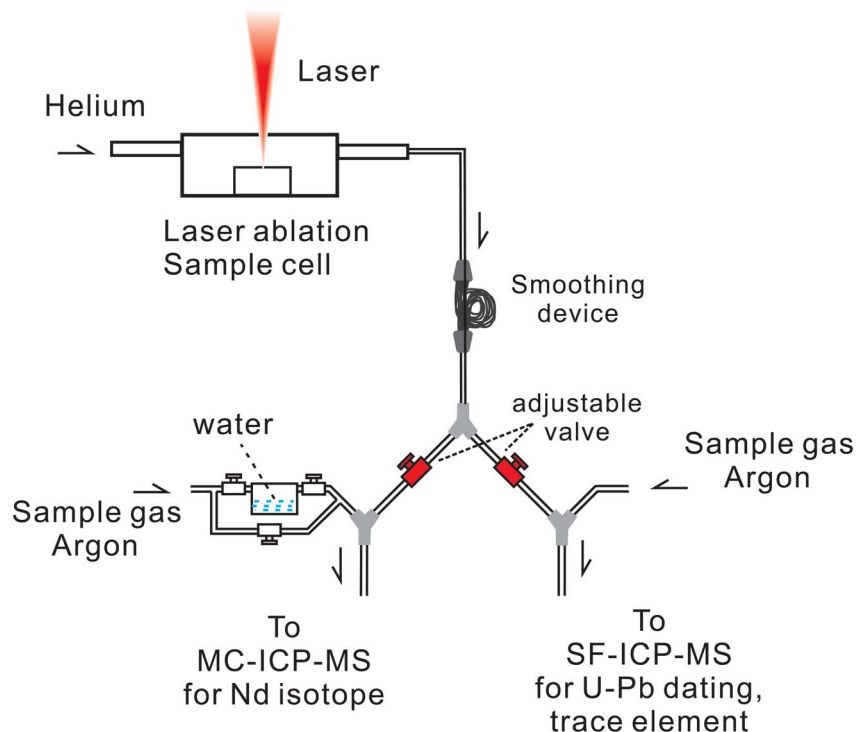
**Fig. 4** Schematic instrumental setup for *in situ* simultaneous measurement of Sm–Nd isotopes, U–Pb dating and trace element concentrations in titanite. Sm–Nd isotopes are measured with MC–ICP–MS and U–Pb dating and trace elements are measured with SF–ICP–MS. Note that the water vapor is introduced into the gas line by the MC–ICP–MS sample gas after the laser ablation chamber, which keeps low oxide yield for U–Pb dating and trace element analyses by SF–ICP–MS. The split ratio between MC–ICP–MS and SF-ICP-MS is controlled by the adjustable valves (in red color).

standard PZHPl for Sr, MKED1 for Yb and the Plesovice zircon standard for Hf, Pb, Th and U. Due to the overlap of NdO with heavy REEs, it is not easy to directly monitor Nd oxide yield. Instead, we measured oxide yield for another REE (Yb), with $^{173}Yb^{16}O$ being free of interference in titanite. Instrumental parameters were carefully tuned for each LA run to optimise results, as summarised in Fig. 3, which indicates that water vapor addition at positions A and B (Fig. 2) have similar effects on elemental sensitivity (Fig. 3a), although sensitivity varies between elements. Sensitivities of Nd, Hf, Th, and U were improved by 10–40% with water vapor, consistent with previous results.[48,50] Water vapor had little effect on Sr and Pb sensitivity. Oxide yields also varied among the elements (Fig. 3b). Sr, Yb, Hf, and Pb oxide yields were low (<0.3%), with or without water vapor, but those of Th and U rose from 3–5% without the addition of water vapor to 20–45% with the addition of water vapor. The similar sensitivity enhancement with addition of water vapor before or after the LA chamber indicates that any sensitivity enhancement is due to water vapor effects in the ICP section. Compared with pure Ar plasma, an Ar–H$_2$O plasma has much higher thermal conductivity[59] resulting in a higher plasma temperature and increased ionisation of refractory elements. The lower sensitivity enhancement for Th and U relative to Nd and Hf (Fig. 3a) may be due to the higher oxide yields of Th and U (Fig. 3b). The presence of water vapor has little effect on the gas blanks for these elements (ESI Table S1†).

Based on these findings, water vapor was introduced into the gas line after the LA chamber in the LASS system to maintain low oxide yields in trace-element analyses by SF–ICP–MS (Fig. 4). The ablated aerosol flow was split into two lines *via* a Y joint. One line mixing with the sample gas from MC–ICP–MS, which flew through the water vapor introduce box and carried water vapor, was transferred to MC–ICP–MS for Sm–Nd isotope analysis. The other line mixing with the sample gas from SF–ICP–MS was transferred to SF–ICP–MS for U–Pb dating and trace element analysis. The split ratio between MC–ICP–MS and SF–ICP–MS was set to 7 : 3 based on our previous study.[45]

### 3.2. Analysis of reference titanites

The Nd contents of the three titanite reference materials (1500–5900 μg g$^{-1}$) required different laser spot sizes to ensure sufficient Nd signal for high-precision Nd isotopic analysis ($^{143}$Nd > 0.6 V). MKED1 was used for external calibration in U–Pb dating, and its laser spot size varied according to that used for the bracketed samples. Results for the standards are summarised in ESI Tables S2–S4,† while Sm–Nd isotopic compositions, U–Pb ages and REE patterns are displayed in Fig. 5 and 6.

T3 has the highest Nd content among the reference materials, requiring a 33 μm laser spot, with 53 analyses yielding $^{143}Nd/^{144}Nd = 0.512612 \pm 0.000036$ (2SD) and $^{147}Sm/^{144}Nd = 0.1986 \pm 0.0041$ (2SD; Fig. 5a and b), within analytical uncertainty of reported MC–ICP–MS data.[8] In the U–Pb diagram, most

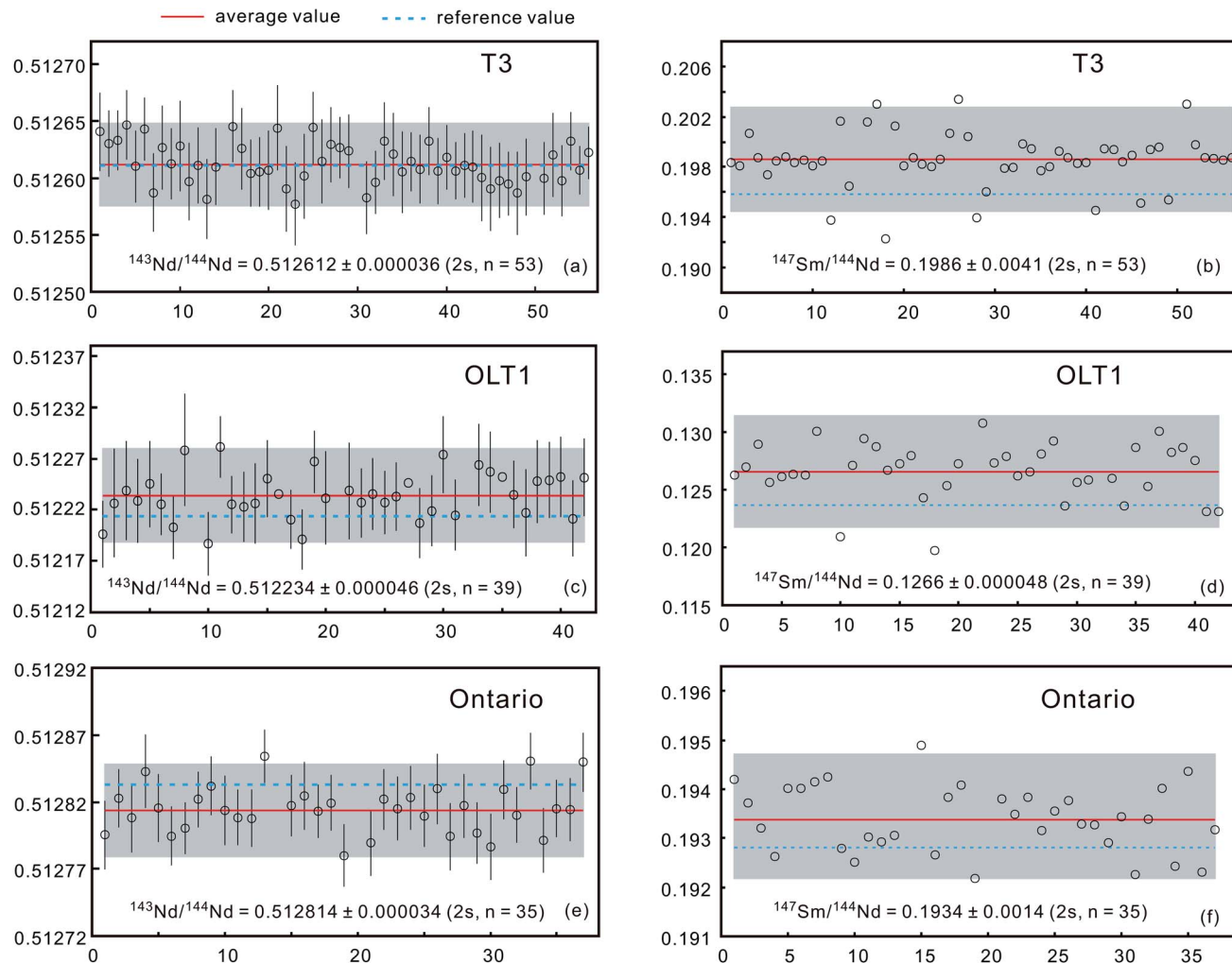**2316** | *J. Anal. At. Spectrom.*, 2021, **36**, 2312–2321

This journal is © The Royal Society of Chemistry 2021

Fig. 5 Analytical results of $^{143}Nd/^{144}Nd$ and $^{147}Sm/^{144}Nd$ for the three reference titanites: T3 (a and b), OLT1 (c and d) and Ontario (e and f). The uncertainty bars are 2 standard error (2SE). The gray areas represent 2 standard deviations (2SD) of each measured sample.

data are clustered on the concordia line (Fig. 6a), consistent with T3 titanite having a very low common-Pb content.[8] The average $^{207}Pb/^{206}Pb$ T3 age is 1134.0 ± 8.7 Ma (2SD; Fig. 4a), consistent with documented values (1125 ± 14 Ma).[8] T3 has high REE contents with and a relatively flat pattern ([La/Lu]$_N$ = 1.2, the subscript $N$ indicates that the ratio is normalized to primitive mantle), with a pronounced Eu trench (Eu/Eu* = 0.19; Fig. 6d).

The OLT1 and Ontario reference materials contain about 2400 μg g$^{-1}$ and 1500 μg g$^{-1}$ Nd, and 45 μm and 60 μm spot sizes were used, respectively. Repeated analyses of OLT1 and Ontario yielded $^{143}Nd/^{144}Nd$ = 0.512234 ± 0.000046 (2SD; $n$ = 39; Fig. 5c) and 0.512814 ± 0.000034 (2SD; $n$ = 35; Fig. 5e), and $^{147}Sm/^{144}Nd$ = 0.1266 ± 0.0048 (2SD; Fig. 5d) and 0.1934 ± 0.0014 (2SD; Fig. 5f), respectively, within uncertainty of reported data.[8] The lower-intercept ages in the TW plots for OLT1 and Ontario were 1015 ± 19 (Fig. 6b) and 1048 ± 24 (Fig. 6c) Ma with average $^{207}Pb$-corrected $^{206}Pb/^{238}U$ ages of 1023.4 ± 12.1 (2SD) and 1044.3 ± 12.5 (2SD) Ma, respectively, consistent with ID–TIMS results (1014.8 ± 2.0 Ma for OLT1 and 1053.3 ± 3.1 Ma for

Ontario).[5,11] OLT1 is enriched in light REEs relative to heavy REEs ([La/Lu]$_N$ = 5.6), and Ontario has a convex REE pattern with a negative Eu anomaly (Eu/Eu* = 0.52; Fig. 6d).

### 3.3. Analysis of titanites from Manjinggou marble

A total of 32 LA spots on 30 titanite grains from the Manjinggou marble were analysed simultaneously for Sm–Nd isotopic and trace-element compositions and U–Pb dating. Since most Manjinggou titanite have low Nd contents (200–400 μg g$^{-1}$), to ensure enough Nd signal intensity, an 82 μm laser spot were used for most grains. Due to the complicated internal structures, 2 analyses involved a 45 μm laser spot. Results are summarised in ESI Table S5.† Most analysed Manjinggou titanites had low common-Pb contents (f$_{206}$ < 0.3%), although two spot analyses had higher values of 2–3%. Barring these two analyses, all spot analyses define a discordant line in the U–Pb concordia diagram (Fig. 7a) with an upper-intercept age of 1864 ± 47 Ma. Our modelling indicates that the analysed Manjinggou titanite underwent 5–15% Pb loss. However, the $^{207}Pb/^{206}Pb$ age is less-affected by Pb loss and all 32 spot analyses yielded a weighted-
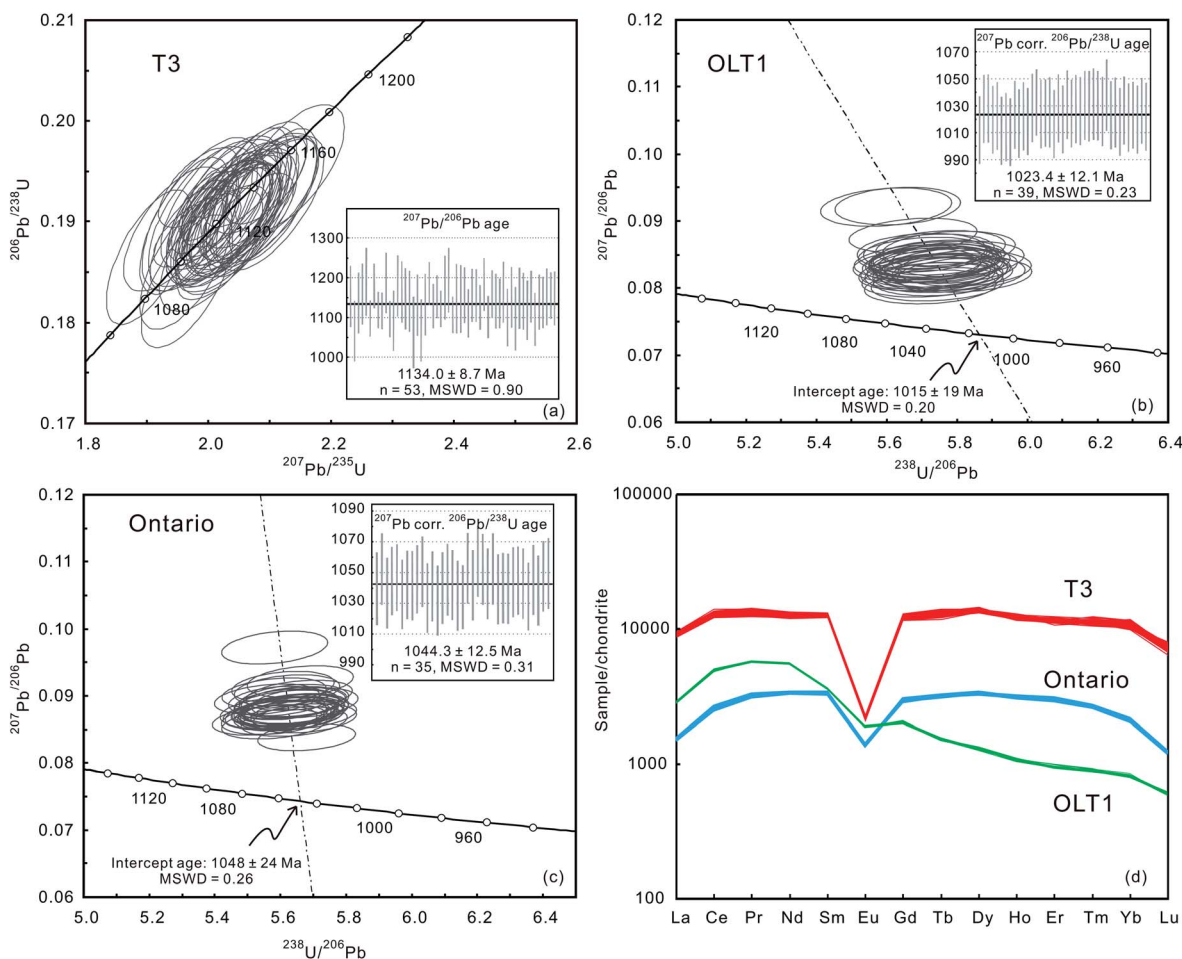
**Fig. 6** Diagrams of U–Pb dating results for the three reference titanites: T3 (a), OLT1 (b) and Ontario (c). (d) Chondrite-normalised REE patterns for these three titanites. The results of T3 are displayed on concordia diagram, and the weighted mean $^{207}Pb/^{206}Pb$ age is calculated based on the $^{207}Pb/^{206}Pb$ apparent age. The results of OLT1 and Ontario are displayed on Tera–Wasserburg diagram, and the weighted mean $^{206}Pb/^{238}U$ ages are corrected the effect of common lead with the $^{207}Pb$ correction method.

mean $^{207}Pb/^{206}Pb$ age of 1860 ± 47 Ma (no common-Pb correction was applied), consistent with the discordant upper-intercept age. A previous study has shown that zircons from the Manjinggou granulites, which are the wall rocks of the Manjinggou marble, have two sets of discordant intercept ages at 1916 ± 30 and 1840 ± 24 Ma, based on zircon cores and rims, respectively,[60] with the older and younger ages likely representing the timing of high-pressure and low-intermediate-pressure granulite-facies metamorphism, respectively.[60] The U–Pb ages of the studied Manjinggou titanite thus may indicate formation during low-intermediate-pressure granulite-facies metamorphism.

The determined $^{143}Nd/^{144}Nd$ and $^{147}Sm/^{144}Nd$ ratios were in the ranges of 0.51152–0.51189 and 0.1246–0.1577, respectively. In the ($^{147}Sm/^{144}Nd$)–($^{143}Nd/^{144}Nd$) diagram, the 32 spot analyses form a Sm–Nd isotopic isochron, yielding an age of 1867 ± 330 Ma (Fig. 7b), consistent with the U–Pb age (although the uncertainty is large). The initial $^{143}Nd/^{144}Nd$ ratio of the Manjinggou titanites was in the range 0.50988–0.51004, yielding an average εNd value of −5.0 ± 1.8 (2SD) and indicating a crustal source.[61] Apart from one spot (180803MJG1-19), all indicate similar trace-element contents and chondrite-normalised REE patterns (Fig. 7c). Spot 180803MJG1-19 indicates higher REE contents and a lower Zr content (287 μg g$^{-1}$) than those of the other spots. Barring this one spot, the analysed Manjinggou titanites have Zr contents of 1675–4162 μg g$^{-1}$ with a generally negative correlation between Zr content and $^{207}Pb/^{235}U$ age (Fig. S2†), possibly resulting from a coupled process involving Pb loss and Zr diffusion after formation. Extrapolation of the relationship between Zr content and $^{207}Pb/^{235}U$ age indicates a titanite Zr content of 1973 ± 75 μg g$^{-1}$ at the time of formation (1864 Ma). A Zr-in-titanite thermobarometer[20] indicates that the Manjinggou titanites were formed at ~807 °C ± 17 °C, assuming a pressure of 10 kbar. These results indicate that the diffusion of Zr should be considered when using the thermobarometer.
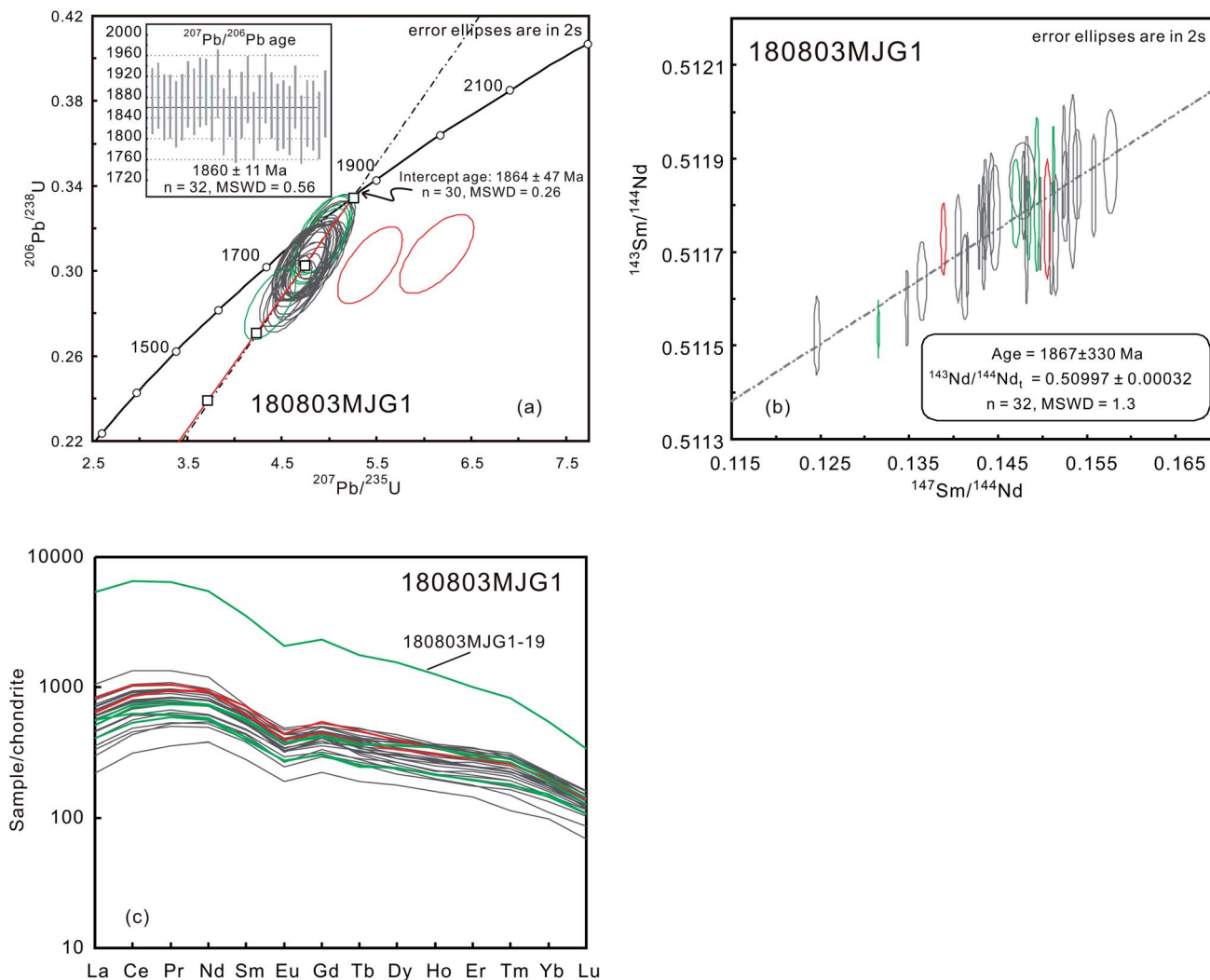
Fig. 7   The measured U−Pb age (a), Sm−Nd isotopes (b) and REE pattern of the titanites from the Manjinggou marble. Data for titanites with high common lead are shown as red symbols. Data shown as green symbols are measured on light-gray domains on BSE image. The red line is the modeling result for Pb loss and the step between two adjacent squares is 10%. The normalization values of chondrite are from Sun and McDonough.[62]

# 4.  Conclusion

Using the LASS technique, an LA system was connected to MC–ICP–MS and SF–ICP–MS systems for simultaneous analysis of Nd isotopic and trace-element compositions and U–Pb dating with a single LA event. The addition of water vapor to the gas stream improved sensitivity to Nd by 40%. To avoid high oxide yields in SF–ICP–MS trace-element analyses, the water vapor was added after ablation. Analytical results for Nd isotopic and trace-element compositions and U–Pb ages of three well-characterised titanite reference materials were consistent with reference values, indicating the applicability of the proposed method. The titanite Nd isotopic composition indicates a crustal origin for the Manjinggou marble. U–Pb ages and temperatures and pressures estimated by a Zr-in-titanite thermobarometer indicate that the studied titanites from the Manjinggou marble formed during low-intermediate-pressure granulite-facies metamorphism, consistent with the granulite wall rocks of the Manjinggou marble.

# Author contributions

L. Zhang conceived the study, made the water vapor introducing device and analyzed the data. L. Zhang and J.-L. Wu collected the sample and prepared the initial draft of the manuscript, tables and figures. Y.-Q. Zhang and Y.-N. Yang conducted sample preparation, mineral separation and part of laser analysis. P.-L. He performed the EPMA analysis. X.-P. Xia and Z.-Y. Ren participated in designing water vapor introducing device and prepared part of the manuscript. All authors contributed to critical discussions and comments on the manuscript.

# Conflicts of interest

There are no conflicts to declare.

## Acknowledgements

## References

1 B. R. Frost, K. R. Chamberlain and J. C. Schumacher, *Chem. Geol.*, 2001, **172**, 131–148.

2 M. J. Kohn, *Rev. Mineral. Geochem.*, 2017, **83**, 419–441.

3 D. J. Cherniak, *Chem. Geol.*, 1993, **110**, 177–194.

4 D. J. Scott and M. R. S. St-Onge, *Geology*, 1995, **23**, 1123–1126.

5 K. J. Spencer, B. R. Hacker, A. R. C. Kylander-Clark, T. B. Andersen, J. M. Cottle, M. A. Stearns, J. E. Poletti and G. G. E. Seward, *Chem. Geol.*, 2013, **341**, 84–101.

6 M. A. Stearns, B. R. Hacker, L. Ratschbacher, D. Rutte and A. R. C. Kylander-Clark, *Tectonics*, 2015, **34**, 784–802.

7 X.-X. Ling, E. Schmädicke, Q.-L. Li, J. Gose, R.-H. Wu, S.-Q. Wang, Y. Liu, G.-Q. Tang and X.-H. Li, *Lithos*, 2015, **220–223**, 289–299.

8 Q. Ma, N. J. Evans, X.-X. Ling, J.-H. Yang, F.-Y. Wu, Z.-D. Zhao and Y.-H. Yang, *Geostand. Geoanal. Res.*, 2019, **43**, 355–384.

9 N. V. Rodionov, E. N. Lepekhina, A. V. Antonov, I. N. Kapitonov, Y. S. Balashova, B. V. Belyatsky, A. A. Arzamastsev and S. A. Sergeev, *Russian Geology and Geophysics*, 2018, **59**, 962–974.

10 Y. Fu, X. Sun, H. Zhou, H. Lin and T. Yang, *Ore Geol. Rev.*, 2016, **77**, 43–56.

11 A. K. Kennedy, S. L. Kamo, L. Nasdala and N. E. Timms, *Can. Mineral.*, 2010, **48**, 1423–1443.

12 J.-W. Li, X.-D. Deng, M.-F. Zhou, Y.-S. Liu, X.-F. Zhao and J.-L. Guo, *Chem. Geol.*, 2010, **270**, 56–67.

13 C. Wanhainen, K. Billstrom, O. Martinsson, H. Stein and R. Nordin, *Miner. Deposita*, 2005, **40**, 435–447.

14 R. M. Essex and L. P. Gromet, *Geology*, 2000, **28**, 419–422.

15 M. J. Kohn and S. L. Corrie, *Earth Planet. Sci. Lett.*, 2011, **311**, 136–143.

16 Q. L. Li, L. Zhao, Y. B. Zhang, J. H. Yang, J. N. Kim and R. H. Han, *Acta Petrol. Sin.*, 2016, **32**, 3019–3032.

17 J. Hammerli, A. I. S. Kemp and M. J. Whitehouse, *Chem. Geol.*, 2019, **524**, 394–405.

18 C. Spandler, J. Hammerli, P. Sha, H. Hilbert-Wolf, Y. Hu, E. Roberts and M. Schmitz, *Chem. Geol.*, 2016, **425**, 110–126.

19 D. J. Cherniak, *Chem. Geol.*, 1995, **125**, 219–232.

20 L. A. Hayden, E. B. Watson and D. A. Wark, *Contrib. Mineral. Petrol.*, 2008, **155**, 529–540.

21 P. L. King, T.-K. Sham, R. A. Gordon and M. D. Dyar, *Am. Mineral.*, 2013, **98**, 110–119.

22 S. Song, J. Mao, G. Xie, L. Chen, M. Santosh, G. Chen, J. Rao and Y. Ouyang, *Miner. Deposita*, 2019, **54**, 569–590.

23 J.-L. Paquette, P. Goncalves, B. Devouard and C. Nicollet, *Contrib. Mineral. Petrol.*, 2004, **147**, 110–122.

24 B. Schoene, J. L. Crowley, D. J. Condon, M. D. Schmitz and S. A. Bowring, *Geochim. Cosmochim. Acta*, 2006, **70**, 426–445.

25 Y.-T. Zhong, B. He, R. Mundil and Y.-G. Xu, *Lithos*, 2014, **204**, 14–19.

26 A. von Quadt, J.-F. Wotzlaw, Y. Buret, S. J. E. Large, I. Peytcheva and A. Trinquier, *J. Anal. At. Spectrom.*, 2016, **31**, 658–665.

27 D. M. Chew, J. A. Petrus and B. S. Kamber, *Chem. Geol.*, 2014, **363**, 185–199.

28 Q.-L. Li, X.-H. Li, Y. Liu, F.-Y. Wu, J.-H. Yang and R. H. Mitchell, *Chem. Geol.*, 2010, **269**, 396–405.

29 X.-H. Li, Y. Liu, Q.-L. Li, C.-H. Guo and K. R. Chamberlain, *Geochem., Geophys., Geosyst.*, 2009, **10**, 1–21.

30 C. D. Storey, T. E. Jeffries and M. Smith, *Chem. Geol.*, 2006, **227**, 37–52.

31 L. Zhang, J.-L. Wu, J.-R. Tu, D. Wu, N. Li, X.-P. Xia and Z.-Y. Ren, *Geostand. Geoanal. Res.*, 2020, **44**, 133–145.

32 Q.-L. Li, X.-H. Li, Y. Liu, G.-Q. Tang, J.-H. Yang and W.-G. Zhu, *J. Anal. At. Spectrom.*, 2010, **25**, 1107–1113.

33 N. T. Kita, T. Ushikubo, B. Fu and J. W. Valley, *Chem. Geol.*, 2009, **264**, 43–57.

34 A. K. Schmitt, K. R. Chamberlain, S. M. Swapp and T. M. Harrison, *Chem. Geol.*, 2010, **269**, 386–395.

35 H. Yuan, S. Gao, X. Liu, H. Li, D. Günther and F. Wu, *Geostand. Geoanal. Res.*, 2004, **28**, 353–370.

36 A. R. C. Kylander-Clark, B. R. Hacker and J. M. Cottle, *Chem. Geol.*, 2013, **345**, 99–112.

37 L.-W. Xie, N. J. Evans, Y.-H. Yang, C. Huang and J.-H. Yang, *J. Anal. At. Spectrom.*, 2018, **33**, 1600–1615.

38 Z. Bao, H. Yuan, C. Zong, Y. Liu, K. Chen and Y. Zhang, *J. Anal. At. Spectrom.*, 2016, **31**, 1012–1022.

39 C. M. Fisher, A. M. Bauer, Y. Luo, C. Sarkar, J. M. Hanchar, J. D. Vervoort, S. R. Tapster, M. Horstwood and D. G. Pearson, *Chem. Geol.*, 2020, **539**, 119493.

40 L. Xie, Y. Zhang, H. Zhang, J. Sun and F. Wu, *Chin. Sci. Bull.*, 2008, **53**, 1565–1573.

41 H.-L. Yuan, S. Gao, M.-N. Dai, C.-L. Zong, D. Günther, G. H. Fontaine, X.-M. Liu and C. Diwu, *Chem. Geol.*, 2008, **247**, 100–118.

42 D. J. Goudie, C. M. Fisher, J. M. Hanchar, J. L. Crowley and J. C. Ayers, *Geochem., Geophys., Geosyst.*, 2014, **15**, 2575–2600.

43 S.-P. Qian and L. Zhang, *Geochem. J.*, 2019, **53**, 319–328.

44 D. L. Tollstrup, L.-W. Xie, J. B. Wimpenny, E. Chin, C.-T. Lee and Q.-Z. Yin, *Geochem., Geophys., Geosyst.*, 2012, **13**, 1–14.

45 L. Zhang, S.-P. Qian, N. Li, L.-B. Hong, Y.-Q. Zhang and Z.-Y. Ren, *Geochem., Geophys., Geosyst.*, 2021, **22**, e2020GC009451.

46 D. Fliegel, C. Frei, G. Fontaine, Z. Hu, S. Gao and D. Günther, *Analyst*, 2011, **136**, 4925–4934.

47 S. Allner, J. Koch, S. E. Jackson and D. Günther, *J. Anal. At. Spectrom.*, 2017, **32**, 2238–2245.

**2320** | *J. Anal. At. Spectrom.*, 2021, **36**, 2312–2321

This journal is © The Royal Society of Chemistry 2021

48 T. Luo, Z. Hu, W. Zhang, D. Günther, Y. Liu, K. Zong and S. Hu, *J. Anal. At. Spectrom.*, 2018, **33**, 1655–1663.

49 T. Luo, Z. Hu, W. Zhang, Y. Liu, K. Zong, L. Zhou, J. Zhang and S. Hu, *Anal. Chem.*, 2018, **90**, 9016–9024.

50 T. Luo, H. Zhao, Q. Li, Y. Li, W. Zhang, J. Guo, Y. Liu, J. Zhang and Z. Hu, *Geostand. Geoanal. Res.*, 2020, **44**, 653–668.

51 N. Lv, K. Chen, Z. a. Bao, K. Wu, D. Lei and H. Yuan, *At. Spectrosc.*, 2021, **42**, 51–61.

52 J.-L. Wu, H.-F. Zhang, M.-G. Zhai, J.-H. Guo, L. Liu, W.-Q. Yang, H.-Z. Wang, L. Zhao, X.-L. Jia and W. Wang, *Precambrian Res.*, 2016, **278**, 323–336.

53 G. Wasserburg, S. Jacousen, D. DePaolo, M. McCulloch and T. Wen, *Geochim. Cosmochim. Acta*, 1981, **45**, 2311–2323.

54 N. T. Kita, T. Ushikubo, B. Fu and J. W. Valley, *Chem. Geol.*, 2009, **264**, 43–57.

55 M. S. A. Horstwood, J. Košler, G. Gehrels, S. E. Jackson, N. M. McLean, C. Paton, N. J. Pearson, K. Sircombe, P. Sylvester, P. Vermeesch, J. F. Bowring, D. J. Condon and B. Schoene, *Geostand. Geoanal. Res.*, 2016, **40**, 311–332.

56 K. R. Ludwig, *Berke Ley Geochronol*. Cen ter Spec. Publ., 2005, pp. 1–71.

57 D. M. Chew, P. J. Sylvester and M. N. Tubrett, *Chem. Geol.*, 2011, **280**, 200–216.

58 J. S. Stacey and J. D. Kramers, *Earth Planet. Sci. Lett.*, 1975, **26**, 207–221.

59 Y. Q. Tang and C. Trassy, *Spectrochim. Acta, Part B*, 1986, **41**, 143–150.

60 J. Wu, H. Zhang, M. Zhai, H. Zhang, H. Wang, R. Li, B. Hu and H. Zhang, *Int. Geol. Rev.*, 2019, **61**, 694–719.

61 A. R. Philpotts and J. J. Ague, *Principles of Igneous and Metamorphic Petrology*, Cambridge University Press, Cambridge, 2nd edn, 2009.

62 S. S. Sun and W. F. McDonough, Chemical and isotopic systematics of oceanic basalts: Implications for mantle composition and processes, in *Magmatism in the Ocean Basins*, ed. A. D. Saunders and M. J. Norry, Geol. Soc. Spec. Publ, London, 1989, vol. 42, pp. 313–345.

This journal is © The Royal Society of Chemistry 2021

*J. Anal. At. Spectrom.*, 2021, **36**, 2312–2321 | **2321**